Design of highly responsive chemiresistor-based sensors by interfacing NiPc with graphene

Check for updates

Daniele Perilli [1,6], Sonia Freddi [2,5,6], Michele Zanotti[2], Giovanni Drera[1,2], Andrea Casotto [2,3], Stefania Pagliara [2], Luca Schio [4], Luigi Sangaletti [2] & Cristiana Di Valentin [1]

Highly sensitive and selective gas-sensing materials are critical for applications ranging from environmental monitoring to breath analysis. A rational approach at the nanoscale is urgent to design next-generation sensing devices. In previous work, we unveiled interesting charge transfer channels at the interface between p-type doped graphene and a layer of nickel phthalocyanine (NiPc) molecules, which we believe could be successfully exploited in gas sensing devices. Here, we have investigated the graphene-NiPc interface's response to adsorbed gas molecules via first-principles calculations. We focused on NH_3 and NO_2 as test molecules, representing electron donors and acceptors, respectively. Notably, we identified the Ni d_z^2 orbital as a key player in mediating the charge transfer and affecting the charge carrier density in graphene. As a proof-of-concept, we then prepared the graphene-NiPc system as a chemiresistor device and exposed it to NH_3 and NO_2 at room temperature. The sensing tests revealed excellent sensitivity and selectivity, along with a rapid recovery time and a remarkably low detection limit.

The development of gas-sensing materials has garnered increasing interest in the scientific community, driven by the growing challenges related to environmental and health issues[1-3], such as air pollution monitoring, food quality tracking, and medical screening campaigns. An ideal sensing material must meet specific requirements, including high sensitivity and selectivity, fast response and recovery time, a noteworthy detection limit, low operating temperature, and cost-effectiveness[4]. Nowadays, commercial state-of-the-art gas sensors are primarily based on metal oxide semiconductor (MOS) systems. While these systems offer considerable sensitivity, they require high operating temperatures[5,6]. This can lead to long-term drift of their sensing properties. In contrast, graphene, reduced graphene oxide (rGO), and other 2D materials, such as transition metal dichalcogenides (TMDs), can operate at room temperature and offer an extremely large set of possible combinations to explore new sensing layers[7]. Furthermore, being 2D, they can be effectively used to explore innovative sensing architectures, such as heterojunction (HJ) and field-effect transistor (FET)[8]. Hence, the need for new systems is more urgent than ever. The rational design of nanoscale architectures requires not only knowledge of all details concerning the morphology and electronic structure of the active material[9] but also an understanding of the sensing mechanism[10], i.e., how the

detectable response originates upon interaction with the target gas molecules.

Given these premises and motivated by the results of our recent work[11], where a graphene-based (Gr) system functionalized with a layer of nickel phthalocyanine (NiPc) molecules exhibited interesting electronic communication channels, we have decided to explore its sensing potential. Such a Gr–NiPc heterointerface, is a model system in terms of its structural simplicity, but it holds significant technological advancements and implications.

Phthalocyanine-based systems have indeed emerged as successful alternatives to MOS for gas-sensing applications. They have been effectively prepared and tested for various reducing and oxidizing gases, demonstrating promising results in terms of sensitivity, selectivity, and lower operating temperatures[12-16]. Phthalocyanines (Pcs) belong to a class of organic molecules composed of four isoindole units linked by nitrogen atoms, forming a macrocyclic structure[10]. The size of the inner cavity allows the hosting of transition metal atoms (M) by forming N–M bonds.

Thanks to their thermal stability, metalated phthalocyanines (MPcs) can be sublimated and deposited onto various types of substrates while preserving their chemical structure. This capability facilitates the creation of

[1]Department of Materials Science, University of Milano-Bicocca, Milano, Italy. [2]I-LAMP and Dipartimento di Matematica e Fisica, Università Cattolica del Sacro Cuore, Brescia, Italy. [3]Department of Chemistry and Biochemistry, University of Notre Dame, Notre Dame, IN, USA. [4]CNR—Istituto Officina dei Materiali (IOM), Laboratorio TASC, Trieste, Italy. [5]Present address: Institute for Photonics and Nanotechnologies (IFN)—Consiglio Nazionale delle Ricerche (CNR), L-NESS Laboratory, Como, Italy. [6]These authors contributed equally: Daniele Perilli, Sonia Freddi. ✉e-mail: luigi.sangaletti@unicatt.it; cristiana.divalentin@unimib.it

heterointerfaces suitable for a wide range of applications, spanning from dye-sensitized solar cells[17], photodynamic therapy[18], energy- and data-storage, spintronics[19], catalysis[20] to gas-sensing[21].

Among the various 2D layers explored as substrates to date, graphene, a monolayer of carbon atoms arranged in a honeycomb lattice, stands out as a superior platform for supporting phthalocyanine molecules[22]. This is primarily because graphene can be obtained with high crystalline quality, controlled morphology, and a large surface area-to-mass ratio[23], allowing a regular and orderly arrangement of atoms or molecules on its surface[24,25]. Notably, non-covalent functionalization, such as when molecules are deposited on graphene, offers the possibility of adjusting its doping level while preserving its transport properties[22]. When it comes to MPcs, heterointerfaces with Gr have been successfully prepared either by thermal evaporation[26–28], or drop-casting methods[29]. However, most of the existing literature has primarily focused on understanding the morphology and the nature of interactions at the interface[30–32], with limited insight into the potential use of such systems as gas sensors. Notably, nickel phthalocyanines (NiPcs) remain the least investigated to date.

In this communication, we present a proof-of-concept study on the potential use of such systems for gas sensing, based on a sophisticated DFT analysis of the details of the interaction with gas molecules at the atomic level and of their implications on the electronic properties of the interface in terms of charge carriers population in the Gr layer, complemented by experimental chemiresistive sensing measurements at decreasing concentration of exposed gas to asses sensitivity and detection limits. Both electron donor and acceptor gases have been used, namely ammonia (NH_3) and nitrogen dioxide (NO_2), because they are historically considered as 'test gases' for the development and testing of new sensors. Furthermore, they hold relevance across various applications, including environmental monitoring, food quality assessment, healthcare, and worker safety[33–37].

In the first stage, state-of-the-art DFT calculations were conducted to elucidate the molecular mechanism of gas adsorption, and to reveal the role played by the phthalocyanine adlayer in the gas sensing mechanism based on the net flow of electrons at the interface. Notably, the Ni d_z^2 orbital emerged as pivotal in the charge transfer mechanism between gas molecules and graphene, facilitating electron charge density movement through hybridization with the frontier molecular orbitals (FMOs) of NH_3 and NO_2 and with the Gr π system. This computational analysis confirmed the great potential of Gr–NiPc systems as gas-sensing materials.

Consequently, in the second stage, we prepared the interface by thermally evaporating NiPc molecules onto a p-type doped Gr layer under ultrahigh vacuum conditions with precise nanoscale control. The characterization by Raman spectroscopy, X-ray photoelectron spectroscopy (XPS), and atomic force microscopy (AFM) confirmed the desired morphology and chemical composition in line with the computational model.

Finally, the prepared Gr–NiPc interface was tested, against a pristine Gr sample, as a chemiresistor when exposed to NH_3 and NO_2 atmospheres. The functionalized system exhibited remarkable sensitivity and a notably low detection limit for both gases, with a sensitivity higher than bare graphene for both target gas molecules.

Results and discussion
First-principles investigation of Gr–NiPc interface
The model system consists of NiPc molecules arranged in a horizontally flat adsorption mode on a free-standing p-type doped Gr layer (see Fig. 1a, b), in agreement with Raman, AFM, and XPS measurements as in our previous study[11]. The resulting molecular height from the Gr layer is 3.48 Å with no corrugation of the Gr layer or distortion of the molecule. Here, we investigate how electron donor/acceptor gas molecules influence the electron interactions at the Gr–NiPc interface, eventually resulting in a detectable response.

First we analyzed the nature of the interaction between Gr and NiPc, which was found to include several contributions: (i) dispersion forces, (ii) hybridization between the Gr π states and NiPc z-component orbitals (as evidenced by small peaks on the Gr curve at the energy positions of molecular peaks and indicated by black arrows in Fig. 2a, b), and (iii) charge transfer from NiPc to the carbon layer (as indicated in Table 1 and confirmed by the Dirac cone shift in Fig. 2b). The origin of this charge transfer lies in the coupling between the Gr π states and the highest occupied molecular orbital (HOMO) of NiPc, which results to be partially emptied (corresponding to the green peak crossing Fermi in Fig. 2a). It is worth noting that the lowest occupied molecular orbital (LUMO) of NiPc is also coupled with the Gr states. In our previous work[11], this coupling between unoccupied states was found to be responsible for the experimentally observed charge transfer processes.

First-principles investigation of NH_3 adsorption and charge transfer mechanism on Gr–NiPc interface
As a next step, we investigated how the interaction with a donor gas, such as ammonia, can impact the Gr–NiPc interface's electronic properties. We know from experiments[11] that exposure to ammonia results in a macroscopic response, namely, an increase in Gr resistance. This increase is associated with a reduction of the density of the majority charge carriers, which, in the system under study, are electronic holes.

The analysis of the electronic structure of the Gr–NiPc system, clearly suggests that the Gr Dirac cone (as indicated by the black curve in Fig. 2a) remains preserved. Since its precise position is very sensitive to any little perturbation[38], particularly in terms of electron charge transfer to or from Gr[39,40], an effective way to computationally monitor variations in the concentration of electronic holes and thus in the Gr resistance, is to examine
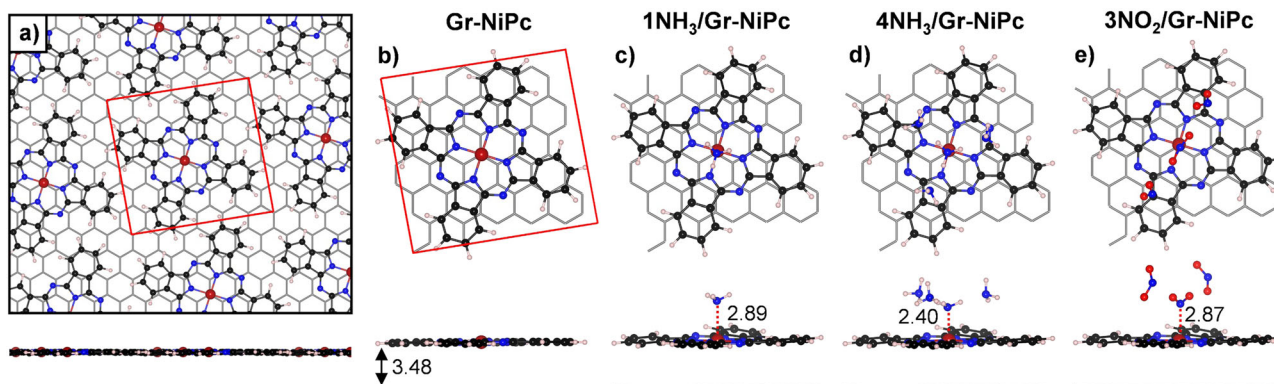

Fig. 1 | Models of the Gr–NiPc interface with and without gas adsorption. Ball-and-stick models (top and side view) of (**a, b**) Gr–NiPc (**c, d**) nNH_3/Gr–NiPc (with $n = 1$ and $n = 4$), and **e** $3NO_2$/Gr–NiPc. Color coding: C atoms in Gr are rendered in dark gray (stick representation); H, C, N, and Ni atoms in NiPc are rendered in white, black, blue, and dark red, respectively (ball-and-stick representation); H, N, and O in adsorbing molecules are rendered in white, blue, and red, respectively. Distances are reported in Å. The supercell is indicated in red (**a, b**).
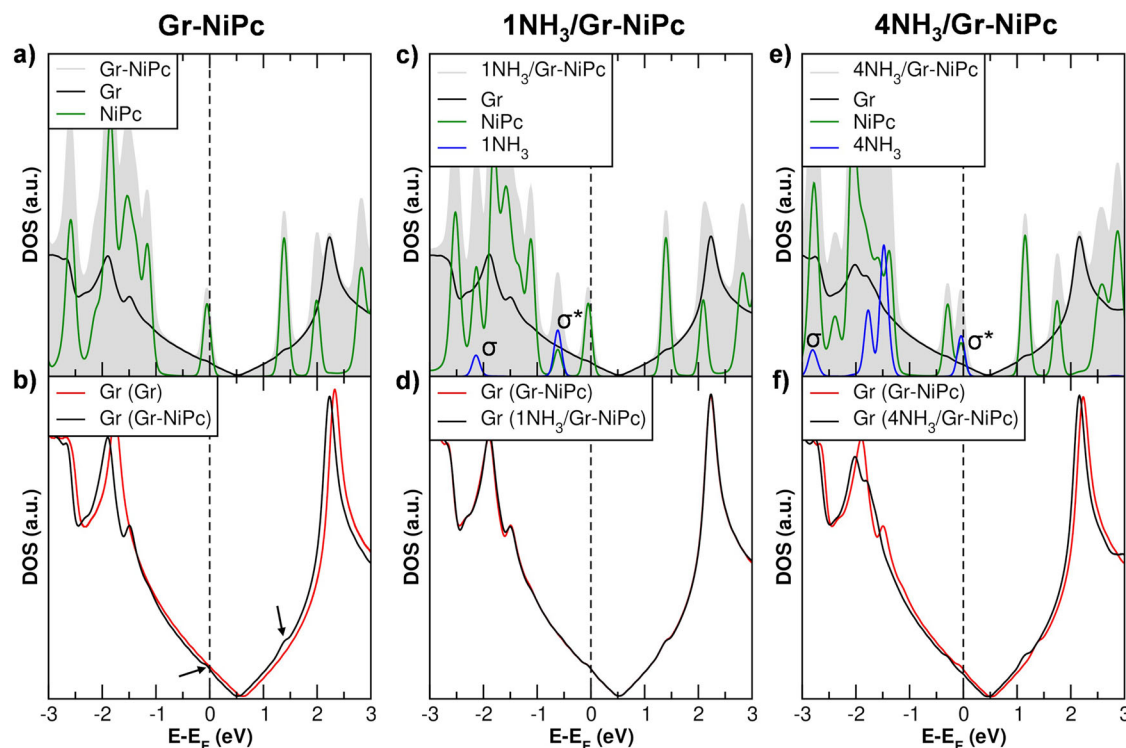
Fig. 2 | Electronic structure of the Gr–NiPc interface with and without ammonia adsorption. Total (TDOS) and projected (PDOS) density of states for (**a**) Gr–NiPc, (**c**) $1NH_3$/Gr–NiPc, and **d**) NH_3/Gr–NiPc. **b** Shows the comparison between the TDOS of pristine Gr (red curve) and the PDOS on Gr for the Gr–NiPc interface (black curve). **d**, **f** display the comparison of the PDOS on Gr between the system with (black curve) and without (red curve) adsorbed NH_3 molecules. The Fermi level is scaled to zero and is indicated by a dashed line. The bonding and antibonding hybrid states discussed in the text are labeled as σ and σ* in (**c**, **e**).

Table 1 | Changes in atomic charges (δq, in e/supercell) with respect to the isolated atom, calculated through Bader analysis for systems shown in Fig. 1 and Supplementary Fig. 3

	δq (e)		
	Gr	**NiPc**	**nNH$_3$**
Gr–NiPc	−0.20	+0.20	–
1NH₃/Gr–NiPc	−0.19	+0.16	+0.03
2NH₃/Gr–NiPc	−0.19	+0.16	+0.03
3NH₃/Gr–NiPc	−0.19	+0.02	+0.18
4NH₃/Gr–NiPc	−0.29	+0.07	+0.22

Negative (positive) values indicate electron charge accumulation (depletion). The second, third, and fourth columns report the charge variation on subgroups of atoms for each system: the entire Gr layer, the NiPc molecule, and the adsorbed NH_3 molecule/s.

whether the Gr Dirac cone results in a shifted position in the presence of adsorbed NH_3 molecules.

We started by considering the scenario where only one NH_3 molecule is adsorbed on the Gr–NiPc. Among the various structures that we could localize (Supplementary Fig. 1), the most stable one is depicted in Fig. 1c. In this case, ammonia lies on top of the Ni site in a N-down configuration, implying a potential interaction involving the N lone pair and the Ni orbitals. To gain deeper insight into this orbital interaction, we analyzed the electronic structure in terms of total (TDOS) and projected (PDOS) density of states. As shown in Fig. 2c, while the HOMO peak of NiPc, crossing Fermi, remains unchanged as it was without NH_3 molecules, the PDOS on NH_3 (blue curve) exhibits two contributions at approximately −2.2 eV and −0.6 eV. These new states result from the mixing of the ammonia sp^3 lone pair and the Ni d_z^2 orbital (Supplementary Fig. 2b–d), thereby creating a new set of bonding (σ) and anti-bonding (σ*) molecular orbitals (see plots in

Supplementary Fig. 2e). Due to this hybridization, only a tiny charge transfer from ammonia to NiPc (approximately 0.03 e, as shown in Table 1) is present, but the Dirac point of Gr does not shift because no additional charge is added to the carbon layer (Fig. 2d). Therefore, we conclude that at this low NH_3 concentration no impact on the electronic properties of the Gr layer can be observed. As a further step, we must consider a larger number of interacting gas molecules.

We have thus added a second ammonia molecule (Supplementary Fig. 3), observing the formation of a hydrogen bond with the first. However, once again, no charge is transferred to Gr, as evidenced by the atomic charges (Table 1) and the position of the Dirac cone (Supplementary Fig. 3). Subsequently, we increased the local coverage further (refer to Supplementary Fig. 3 and Table 1 for details on the case with three ammonia molecules). Notably, with four interacting ammonia molecules, the system finally responds to the gas. This configuration corresponds to a reasonable number of molecules that match the experimental conditions of our previous works[11,38] (approximately 0.2/3.6 molecules per cell). When looking at the gas molecule arrangement (Fig. 1d), we note that one ammonia molecule is positioned on top of the Ni site in a N-down configuration, while the other three NH_3 molecules are surrounding the first adsorbed one, each establishing one hydrogen bond as H acceptors. The shorter N–Ni distance (2.40 Å compared to 2.89 Å in the low coverage case discussed above with only one NH_3 molecule) suggests a stronger NH_3–NiPc interaction. We wish to note that, interestingly, a similar cluster of ammonia molecules has been recently proposed to explain the experimentally observed high NH_3-uptake capacity of rather different systems, i.e. metal-organic polyhedra (MOP)[41].

When analyzing the computed density of states at higher NH_3 density (Fig. 2e, f), we observe a downward shift in the position of the Dirac cone as compared to the system without adsorbed NH_3 molecules (black and red curves in Fig. 2f). This shift must result from the filling of graphene empty states, causing a reduction in the number of holes, and its direction agrees

with the experimental observation of an increase in graphene resistance upon NH$_3$ exposure[11,38]. In the following discussion, we will try to identify the key factors contributing to this observed shift.

Conversely from the low NH$_3$ coverage regime, several notable differences are observed. Firstly, the NH$_3$ σ* state is at a higher energy level compared to the HOMO of NiPc, and it was found to become partially empty (see Fig. 2e). In principle, one might expect both σ and σ* hybrid states to be filled since they originate from two filled orbitals, namely the sp^3 lone pair of NH$_3$ and Ni d_{z^2} of NiPc. However, in this case, the antibonding state (σ*) is partially empty (as indicated by the blue peak crossing Fermi in Fig. 2e). This partial emptiness is caused by an electron charge transfer to Gr, leading to the downshifting of the Dirac point of Gr, which is clearly observed. The reason behind this transfer can be attributed to the nature of the Ni d_{z^2} orbital, which is found to be coupled also with the metallic Gr π system. This coupling is similar to the broadening experienced by sharp atomic or molecular states of adsorbates when they interact with s states of metal surfaces[42]. The open question is: why a cluster of ammonia molecules is required to shift the Gr Dirac cone, or, in other words, what is the role of surrounding NH$_3$ molecules? This still needs to be clarified.

Based on the projected density of states (PDOS) shown in Supplementary Fig. 4, the ammonia sp^3 state that interacts with the Ni d_{z^2} orbital belongs to the ammonia molecule orienting the N atom toward the Ni atom (H-donor molecule). However, the charge transfer to Gr is made possible through the contributions of the other three surrounding (H-acceptor) ammonia molecules, which interact with the central ammonia molecule via hydrogen bonds. As shown in Supplementary Fig. 5, in the absence of Gr–NiPc, these hydrogen bonds destabilize the surrounded (H-donor) ammonia molecule, causing a positive shift of the N lone pair energy level that is quite proportional to the number of H-bonded molecules, going from 1 to 3 (see inset on the right of Supplementary Fig. 5). This energy increase is responsible for the charge transfer to Gr, as schematically represented in Fig. 3 and discussed below.

The d-band model, previously introduced in the literature to elucidate the bonding interaction between adsorbates and transition-metal surfaces[42], can be also applied to the current case. In its original formulation, this model assumes that the coupling between the adsorbate valence states and the d states of the metal surface results in the formation of bonding and antibonding states. The strength of the interaction is determined by the extent of electron filling of the antibonding states, or, in other words, the energy position of these states in relation to the Fermi level. As the antibonding states lie above the d states, the energy position of the d states relative to the Fermi level serves as a reliable initial indicator of the bond strength. The greater the energy level of the d states relative to the Fermi level, the higher the energy of the antibonding states, resulting in a stronger bond.

In the present situation, donor gas molecules (NH$_3$) interact with an adsorbed molecule (NiPc) on Gr. Moving from left to right in Fig. 3, after the deposition of NiPcs on Gr and formation of the Gr–NiPc interface, the Ni d_{z^2} state of the gas-phase NiPc couples with the Gr π states, resulting in a downshift and broadening of the Ni orbital. On the other side (the right side of Fig. 3), the energy position of the N lone pair of the H-donor ammonia molecule in the gas phase depends on the number and position of surrounding ammonia molecules (H-acceptors), as discussed above.

When ammonia molecules are put on Gr–NiPc (as in Supplementary Fig. 3), the N lone pair of the adsorbing ammonia molecule mixes with the Ni d_{z^2} state of Gr–NiPc, creating a new set of σ bonding and σ* antibonding orbitals. The positive shift in the energy level of the N lone pair of the NH$_3$ molecule adsorbing on Ni, when surrounded by other 3 NH$_3$ H-acceptor molecules, reflects in a positive shift in the energy of the resulting antibonding σ* molecular orbital (of Ni–NH$_3$), becoming sufficiently high to donate to the NiPc and, only in the case of 4 NH$_3$, even to the Gr layer.

In particular, with a single ammonia molecule, the energy alignment between the NH$_3$ HOMO and the empty states of the Gr–NiPc interface prevents electron transfer to both NiPc and graphene (see top panel of Supplementary Fig. 6). With two or three ammonia molecules, the increase of the interacting NH$_3$ HOMO energy in Supplementary Fig. 5 (and
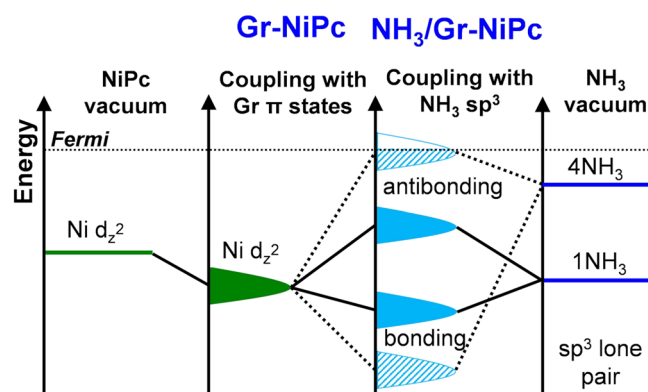

Gr-NiPc   NH$_3$/Gr-NiPc

Fig. 3 | Schematic representation of orbital mixing upon ammonia adsorption. Schematic representation of the orbital interactions at the nNH$_3$/Gr–NiPc interface, with n = 1 or 4. The process begins with the coupling of Ni d_{z^2} (from the gas-phase NiPc molecule) with Gr π states, followed by the mixing with the sp^3 lone pair (HOMO) of the adsorbing NH$_3$ molecule. In the case of 4NH$_3$, only the ammonia molecule placed on top of Ni is considered for the scheme. This sequence results in the formation of a bonding (σ) and antibonding (σ*) state. The degree of filling of the antibonding state (σ*) is indicated by its position with respect to Fermi (black dashed line).

consequently of the σ* orbital formed upon adsorption on NiPc in Supplementary Fig. 6) is sufficient to observe an electron transfer to Pc but not to graphene (see second and third panels of Supplementary Fig. 6). Only with four ammonia molecules, the energy rise of the interacting NH$_3$ HOMO in Supplementary Fig. 5 (as well as the σ* state in Supplementary Fig. 6) is sufficiently large to allow electron transfer from ammonia to both NiPc and graphene. We expect that the higher the σ* antibonding state the more electron charge density can be transferred to NiPc and Gr π system, reducing the number of Gr hole charge carriers.

First-principles investigation of NO$_2$ adsorption and charge transfer mechanism on Gr–NiPc interface

Now that the sensing mechanism for a donor molecule has been outlined, we proceed to investigate the mechanism involving an acceptor species, like NO$_2$. Therefore, in the following, we explore whether the concepts developed for NH$_3$ can be applied or adapted to NO$_2$.

Unlike NH$_3$, nitrogen dioxide is a spin-polarized molecule with a ground state multiplicity of a doublet. As illustrated in Supplementary Fig. 7a, the unpaired electron occupies a molecular orbital with a π* character (HOMO), which is fully delocalized on the molecule. Its empty counterpart, in the spin-down channel, is the LUMO of the molecule. We expect this to become filled upon interaction with Gr–NiPc, because of the NO$_2$ electron-acceptor nature. Since in this scenario, Gr–NiPc will transfer electrons to NO$_2$, we decided to consider a lower degree of p-type doping of the Gr layer, compared to that used in the case of ammonia in the previous section. This is necessary because if Gr is too electron-poor, it cannot transfer charge to NO$_2$. Due to the reduced p-type doping, here we do not observe electron transfer from NiPc to Gr as we did before (see Table 2), and, the corresponding NiPc HOMO level is fully occupied below Fermi (Fig. 4a, b).

Next, we start to adsorb one NO$_2$ molecule on the Gr–NiPc interface, and we identified two nearly isoenergetic minimum energy structures (Supplementary Fig. 8). In these minima, the molecule is placed on the Ni site in either an N-down (slightly more stable) or O-down configuration. Examining the projected density of states (PDOS) in Fig. 4c, we observe mixing between the LUMO of NO$_2$ and the NiPc orbitals, as indicated by the two blue peaks (arrows). According to Supplementary Fig. 9, due to this mixing, the Ni d_{z^2} orbital is no longer fully occupied transferring some electron charge density to the LUMO of NO$_2$, becomes partially occupied. This charge transfer is confirmed by computed Bader atomic charge values

(Table 2), showing that Gr–NiPc transfers approximately 0.10 e to NO_2. In contrast to the ammonia case, Gr is now playing an active role in the charge transfer even at low coverage, as demonstrated by the downshift of its Dirac cone (Fig. 4d).

Similar to the case of ammonia, we expanded our investigation to include a larger number of gas molecules by introducing two additional NO_2 molecules surrounding the one orienting the N toward Ni (see Fig. 4e). This choice is based on the fact that the N-down molecule interacting with Gr–NiPc can be directly coordinated by two other molecules, resulting in a cluster of three molecules. Upon analyzing the density of states (Fig. 4f), we observed a situation qualitatively similar to the lower coverage case, although with a larger quantified charge transfer of approximately 0.16 e. The overall electronic effect aligns well with the scheme presented in Fig. 3, with the only distinction being that it is now the LUMO of the gas molecule that hybridizes with the Ni d_z^2 orbital. As a result of this, a modified version of the previous scheme is presented in Fig. 5. Since no significant differences in the LUMO position are registered upon the increase of NO_2 molecules

(see Supplementary Fig. 9a, b), in contrast with what was observed for ammonia gas, here we have only considered the low coverage regime, with one NO_2 molecule, in the scheme.

In this case, the mixing involves one filled (Ni d_z^2) and one empty state (LUMO of NO_2), creating new bonding and antibonding pair states. The antibonding state is expected to be empty, but due to its energy position, it receives electrons and becomes partially filled. We highlight that the degree of filling of the σ* antibonding orbital is directly related to the electron charge transfer from Gr–NiPc to NO_2, computed to be 0.10 e according to the Bader scheme (refer to Table 2). Since these electrons are removed from the Gr, we can clearly explain the decrease in resistance observed experimentally upon NO_2 exposure[11]: Gr becomes more p-doped, and the density of its majority charge carriers (holes) increases. Similar to the ammonia case, this mechanism is possible thanks to the hybridized nature of the Ni d_z^2 orbital of NiPc, which is mixed with the Gr states.

Comparative analysis of the sensing performance by pristine vs NiPc-functionalized graphene

In this section, we prove that functionalization with NiPc indeed improves sensing performance compared to pristine Gr. Starting with the ammonia case, we explored scenarios where one and four molecules adsorb directly on the bare Gr surface (see Supplementary Fig. 10a, b for geometry details). At low coverage, graphene does not respond to the gas molecule, as illustrated by Supplementary Fig. 10e, where the position of the Dirac cone remains unchanged in the presence of the adsorbed gas. In contrast, the situation alters when the number of interacting molecules increases to four (Supplementary Fig. 10b), and the Dirac cone shifts due to charge transfer to Gr (see Supplementary Fig. 10f and Supplementary Table 1). Although the situation may seem similar to the Gr–NiPc system, two significant differences emerge. Firstly, the adsorption of

Table 2 | Changes in atomic charges (δq, in e/supercell) with respect to the isolated atom, calculated through Bader analysis for systems shown in Fig. 1e and Supplementary Fig. 8

	δq (e)		
	Gr	**NiPc**	**nNO$_2$**
Gr–NiPc	−0.01	+0.01	–
1NO$_2$/Gr–NiPc	+0.03	+0.07	−0.10
3NO$_2$/Gr–NiPc	+0.06	+0.10	−0.16

Negative (positive) values indicate electron charge accumulation (depletion). The second, third, and fourth columns report the charge variation on a subgroup of atoms for each system: the whole Gr layer, the NiPc molecule, and the adsorbed NO$_2$ molecule/s.
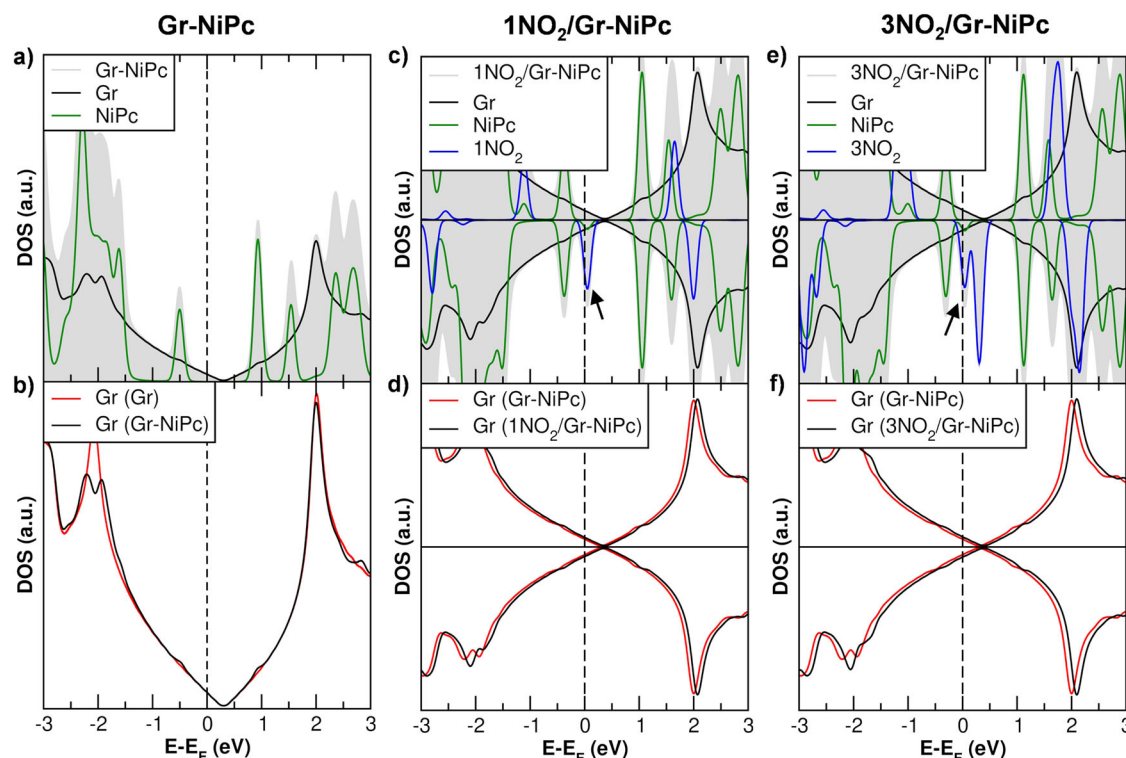

Fig. 4 | Electronic structure of the Gr–NiPc interface with and without NO$_2$ adsorption. Total (TDOS) and projected (PDOS) density of states for (**a**) Gr–NiPc, **c** 1NO$_2$/Gr–NiPc, and **d** 3NO$_2$/Gr–NiPc. **b** Shows the comparison between the TDOS of pristine Gr (red curve) and the PDOS on Gr for the Gr–NiPc interface (black curve). **d**, **f** display the comparison of the PDOS on Gr between the system with (black curve) and without (red curve) adsorbed NO$_2$ molecule/s. The Fermi level is scaled to zero and is indicated by a dashed line. Black arrows in (**c**, **e**) indicate the LUMO of NO$_2$ partially filling due to the charge transfer from the Gr–NiPc system. The antibonding hybrid state discussed in the text is indicated by a black arrow in panels (**c**, **e**).
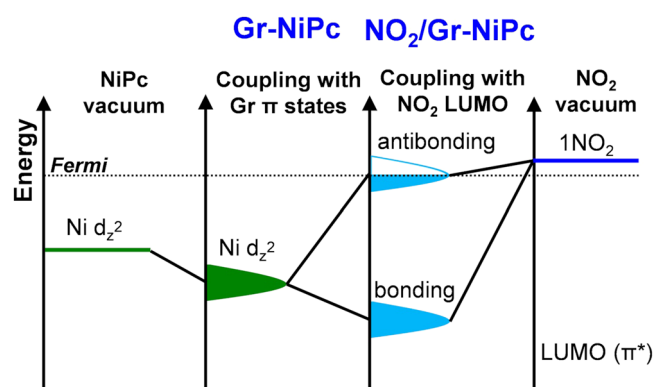
Fig. 5 | Schematic representation of orbital mixing upon NO₂ adsorption. Schematic representation of the orbital interactions at the $1NO_2$/Gr–NiPc interface. The process begins with the coupling of Ni d_{z^2} (from the gas-phase NiPc molecule) with Gr π states, followed by the mixing with the empty LUMO of the adsorbing NO_2 molecule. This sequence results in the formation of a bonding (σ) and antibonding (σ*) state. The degree of filling of the antibonding state (σ*) is indicated by its position with respect to Fermi (black dashed line).

ammonia is more favorable in the presence of NiPc than directly on Gr, -1.58 eV vs -1.22 eV, respectively. Therefore, the likelihood of ammonia molecules interacting with Gr–NiPc will be higher. Secondly, the amount of charge transferred to graphene from ammonia is greater in the case mediated by NiPc, as observed in the values reported in Supplementary Table 1.

Consequently, the NiPc functionalization will enhance the sensing performance of graphene, both by increasing the probability of interaction between Gr–NiPc and NH_3 and by improving the charge transfer to Gr.

In the case of NO_2, (refer to Supplementary Fig. 10c, d for geometry details), bare Gr demonstrates to be influenced even with a single molecule, potentially yielding a higher response than in the non-functionalized case, due to increased charge transfer from Gr (Supplementary Table 1). However, NO_2 adsorbs more strongly on Gr–NiPc (-0.34 eV) than on Gr (-0.21 eV), making the former system more effective under working conditions. The -0.13 eV energy difference at room temperature enhances the probability of NO_2 molecules interacting with the surface, staying for a longer time, facilitating a more substantial charge transfer from Gr, and resulting in a greater response.

Moving to the higher gas coverage (Supplementary Fig. 10d), the adsorption energy is practically identical to Gr–NiPc, with a slightly greater electronic charge transfer to NO_2: 0.21 e for Gr and 0.16 e for Gr–NiPc. However, achieving high coverage in both pristine and NiPc-functionalized cases is improbable due to the small adsorption energy value (≈ -0.5 eV), significantly offset by entropic loss in adsorbing three gas-phase molecules. Consequently, we can conclude that, unlike in the case of ammonia, where four molecules were required, the gas response here is attributed to the interaction with a single molecule of NO_2 per active site, and it is more favorable in the case of Gr–NiPc with respect to Gr.

Proof-of-concept experiment: synthesis and characterization of Gr–NiPc

The computational study presented in the section above suggests that the Gr–NiPc heterointerface is a promising system to be used in gas-sensing chemiresistor devices. In this section we will present a proof-of-concept study where the material has been prepared and tested for both NH_3 and NO_2 detection, to evaluate its sensitivity and detection limit.

First, we synthesized the Gr–NiPc interface using the same procedure as in our previous work[11]. Nickel phthalocyanine powder was sublimated under ultra-high vacuum (UHV) conditions using a custom-made thermal evaporator to functionalize a graphene sample on a 4H–SiC substrate (GraphenSic, see the "Methods" section for additional information). As will

be proved by the characterization presented in the following, with this approach and thanks to the controlled deposition, we can achieve an ideal interface that closely resembles our computational model. Additional information about the sublimation process can be found in the "Sample preparation and characterization" section.

Raman spectroscopy, atomic force microscopy (AFM), and X-ray photoelectron spectroscopy (XPS) measurements were conducted on both pristine graphene (Gr), serving as a reference system, and the functionalized graphene sample (Gr–NiPc) to assess their chemical and morphological composition.

Representative Raman spectra of these samples are reported in Fig. 6a. In the pristine graphene layer (Gr, red spectrum), the typical graphene bands are clearly observed. These include the G band at 1580 cm^{-1}, attributed to the C–C stretching of sp^2 hybridized carbon atoms in the graphene lattice, and the 2D band at 2660 cm^{-1}, associated with a second-order Raman scattering process related to the breathing mode of carbon atoms in the graphene plane[43]. The substrate's contribution is evident due to the presence of a broad band at 1530 cm^{-1} and a minor peak at 1700 cm^{-1}, which can be attributed to the SiC layer (also refer to Supplementary Fig. S11)[44].

In both the pristine graphene (Gr, red spectrum) and the functionalized Gr–NiPc sample (blue spectrum), the characteristic G and 2D bands are observed. Additionally, the Gr–NiPc spectrum reveals the presence of NiPc molecules, characterized by the main peak at 1550 cm^{-1} (also see Supplementary Fig. S11). The shape of the Raman 2D band serves as a valuable tool for determining the graphene layer's structure[45], with a monolayer exhibiting a distinct and intense 2D band. Consequently, Raman maps of this band were acquired on various areas of the samples, primarily focusing on the pristine sample. The results regarding the peak's shape confirm that, as certified by the producer, approximately 25% of the sample consists of non-monolayer graphene.

AFM measurements were conducted to assess the sample surface quality. The topographic image obtained from the pristine sample (Fig. 6b) reveals a superposition of different layers and their edges. This observation aligns with both the producer's certification and the analysis of Raman maps. On the Gr–NiPc surface, small aggregates are visible (Fig. 6c). These tiny NiPc molecule aggregates typically form when the total amount of NiPc surpasses that required for a monolayer[11].

Therefore, it is plausible to propose that a monolayer of NiPc initially covers the entire graphene layer, with NiPc molecules subsequently aggregating on this monolayer, forming the visible structures. To support this hypothesis, the surface roughness, providing insights into the surface nature, was evaluated using several AFM images of the samples. The pristine layer exhibited an average roughness of 72 pm. For the Gr–NiPc sample, the average total roughness was measured at 112 pm. However, when the aggregates were excluded, and only the layer beneath was considered, the roughness was 93 pm. The higher roughness observed for the layer beneath the aggregates, in comparison to the pristine layer, suggests the presence of a NiPc monolayer under the aggregates.

Finally, XPS analysis further confirmed the presence of the NiPc molecules in the functionalized layer and assessed the chemical composition of both samples, as shown in Supplementary Fig. S12. A detailed discussion of the XPS core level spectra is available in Section 3 of Supplementary Information.

Proof-of-concept experiment: gas sensing measurements of Gr–NiPc vs Gr

After characterization, both Gr and Gr–NiPc samples were mounted on a specially designed platform for simultaneous sensing response measurements.

Exposure times have been set at 3 min and 5 min, for ammonia and nitrogen dioxide gases, respectively. These timescales are defined by the geometry of the chambers and the gas fluxes exploited for the measurements, as reported in the SI file. The minimum time required for the detection of NH_3 and NO_2 is influenced by several parameters, including
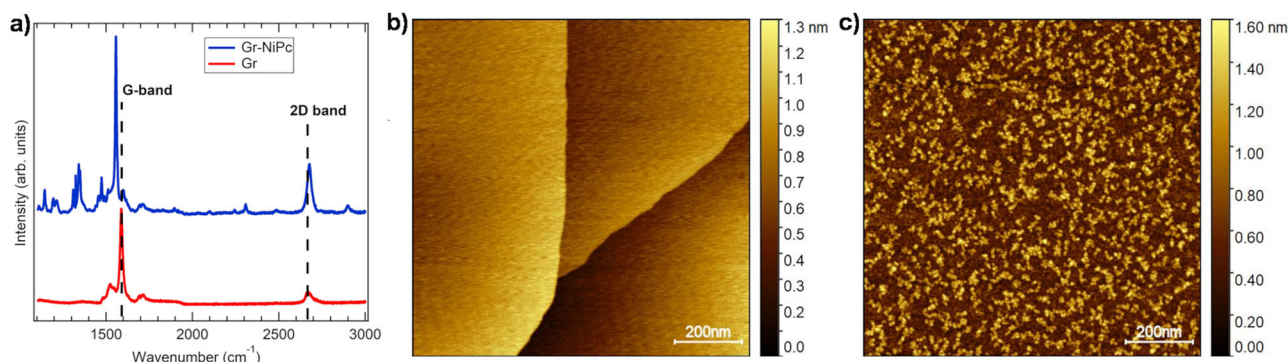
Fig. 6 | Raman and atomic force microscopy characterization of the Gr–NiPc system. a Representative Raman spectra of the pristine graphene (red curve) and the functionalized graphene layer, i.e., Gr–NiPc (blue curve). Representative AFM topography images were collected on Gr, (**b**) and Gr–NiPc (**c**).

these two[46]. In our operating conditions, 3 min and 5 min can be considered as the minimum time values required for correct detection. Both time lengths are compatible with real applications; in particular, they are in the typical time of interest for breathomics applications, since it has been demonstrated[47] that the patient classification could be reached using an e-nose with an exposure to the patient's breath within such a time scale.

Details on gas measurements and the setup can be found in the SI file. Fig. 7a, b illustrates the typical sensor response during exposures to ammonia and nitrogen dioxide. An increase in resistance is observed during ammonia exposure, while resistance decreases during nitrogen dioxide exposure, consistent with the *p*-type nature of both samples. Both sensors exhibit a rapid response (for NH_3: 137 s and 132 s, for Gr and Gr–NiPc respectively; for NO_2: 156 s and 150 s, for Gr and Gr–NiPc), with Gr–NiPc showing slightly faster recovery, especially during ammonia exposure. The observed response and recovery times align with those reported in the literature (see Supplementary Table 2). In general, recovery from exposure to nitrogen dioxide is slower compared to ammonia for both sensors. This slower recovery can be attributed to various factors, including the distinct nature of the two gases and the higher reactivity of nitrogen dioxide with nanocarbon surfaces. Nitrogen dioxide desorption is more challenging, resulting in a slower recovery, a phenomenon well-documented, particularly in the case of CNTs[4].

Lastly, the exposures for both sensors are presented within the same resistance range, emphasizing the greater resistance change observed in the Gr–NiPc sample compared to the pristine layer for both tested gases.

Multiple exposures at various concentrations were carried out for both gases to construct the calibration curves, as shown in Fig. 7c, d. Both sensors exhibit a sublinear behavior, which is typical of carbon-based materials[11,48], and the functionalization improves the response to both ammonia and nitrogen dioxide. A Freundlich isotherm ($\frac{\Delta R}{R_0} = A[gas]^{pow}$) was employed to fit the data, and the fitting parameters are presented in the Supplementary Table 3.

The data from the calibration curves were also used to benchmark the sensitivity parameter (*S*), defined as $S = \frac{(\frac{\Delta R}{R_0} \times 100)}{[gas]}$, against literature data on graphene-based chemiresistor sensors[21,38,48–71].

It is worth underlining that only works clearly reporting sensor response/sensitivity and gas concentration tested, operating at room temperature and without annealing of UV irradiation, were considered for this benchmarking. Figure 8 shows the sensitivity comparison, illustrates the sensitivity comparison, featuring the best-performing sensor from each paper. It is evident that the sensors presented here exhibit the highest sensitivity to both ammonia and nitrogen dioxide exposures.

Finally, it is worth mentioning that in this study, exposures to both tested analytes were conducted in a low concentration range. This is of utmost importance for potential applications where the sensors need to detect low- or sub-ppm concentrations of analytes. Previous studies have primarily focused on the 5–1000 ppm range for ammonia[50–52,54,55,57,58,60] and

3–100 ppm for nitrogen dioxide[64,65,67,69,70] (refer to Supplementary Table 2 for additional details).

Other essential parameters of gas sensors include the detection limit, which is the lowest concentration of analytes that the sensors can detect, and selectivity. The detection limit (*dl*) was calculated using the formula: $dl = \frac{3[gas]}{(\frac{(R-R_0)}{\sigma})}$[72], where σ represents the fluctuation of the electrical signal. It is noteworthy that the functionalized layer exhibits a lower detection limit compared to the pristine one Specifically, the detection limit for nitrogen dioxide is 75 ppb for Gr–NiPc and 100 ppb for Gr. For ammonia, the detection limits are 3 ppb for Gr–NiPc and 6 ppb for Gr. These detection limits rank among the best reported in the literature, particularly in the case of ammonia (see Supplementary Table 2 for reference).

Selectivity was evaluated by exposing the sensor to different gases known to be common major interfering[61]. The results are presented in Supplementary Fig. S13, showing no significant response to benzene and 2-propanol exposures. Additionally, responses were essentially negligible for acetone, ethanol, and water, even at high concentrations. Notably, tests involving water vapor exposure were conducted to meet the requirements of various applications, including breathomics, where sensors need to operate effectively and remain stable in the presence of 100% humidity. The responses to water molecules clearly indicate that functionalization enhances selectivity and stability against these potentially interfering substances. However, it's noteworthy that the response of the Gr–NiPc sensor is lower compared to that of the Gr layer when exposed to 500 ppm of water.

The selectivity of single chemiresistors is not commonly probed with a gas mixture but it is assessed by registering a high sensitivity to the target gas molecule against a low sensitivity to other possible interfering gases in separated measurements (see, e.g., refs. 73–75). Here, we tried to check the effect of a background of interfering gas by considering a simultaneous exposure to ammonia and another gas species, which is known to be an interferent in breath analysis. With the exception of water (measured as relative humidity), interfering gases in breathomics are usually found at concentrations lower than or comparable to that of the target gas molecules[36]. Therefore, exposures to a mixture of ammonia and acetone, in similar concentrations, have been performed, to prove the capability of both proposed sensors to recognize and detect ammonia solely. The response towards the mixture is indeed the same as the response towards the sole ammonia, as can be observed in Supplementary Fig. S14. This result is expected also in the case of ammonia + ethanol, ammonia + 2-propanol, and ammonia + benzene since the response of the sensors towards these interfering gases in concentration relevant for real applications is virtually completely negligible (Supplementary Fig. S13).

Another approach to assess the selectivity of a sensor in the simultaneous presence of more gases is to expose electronic noses (e-noses) to gas mixtures[71,76,77]. Along this line, here we have also performed principle component analysis (PCA) on a dataset obtained by exposing an e-nose (made of the proposed Gr-based sensors and the RH commercial sensor,
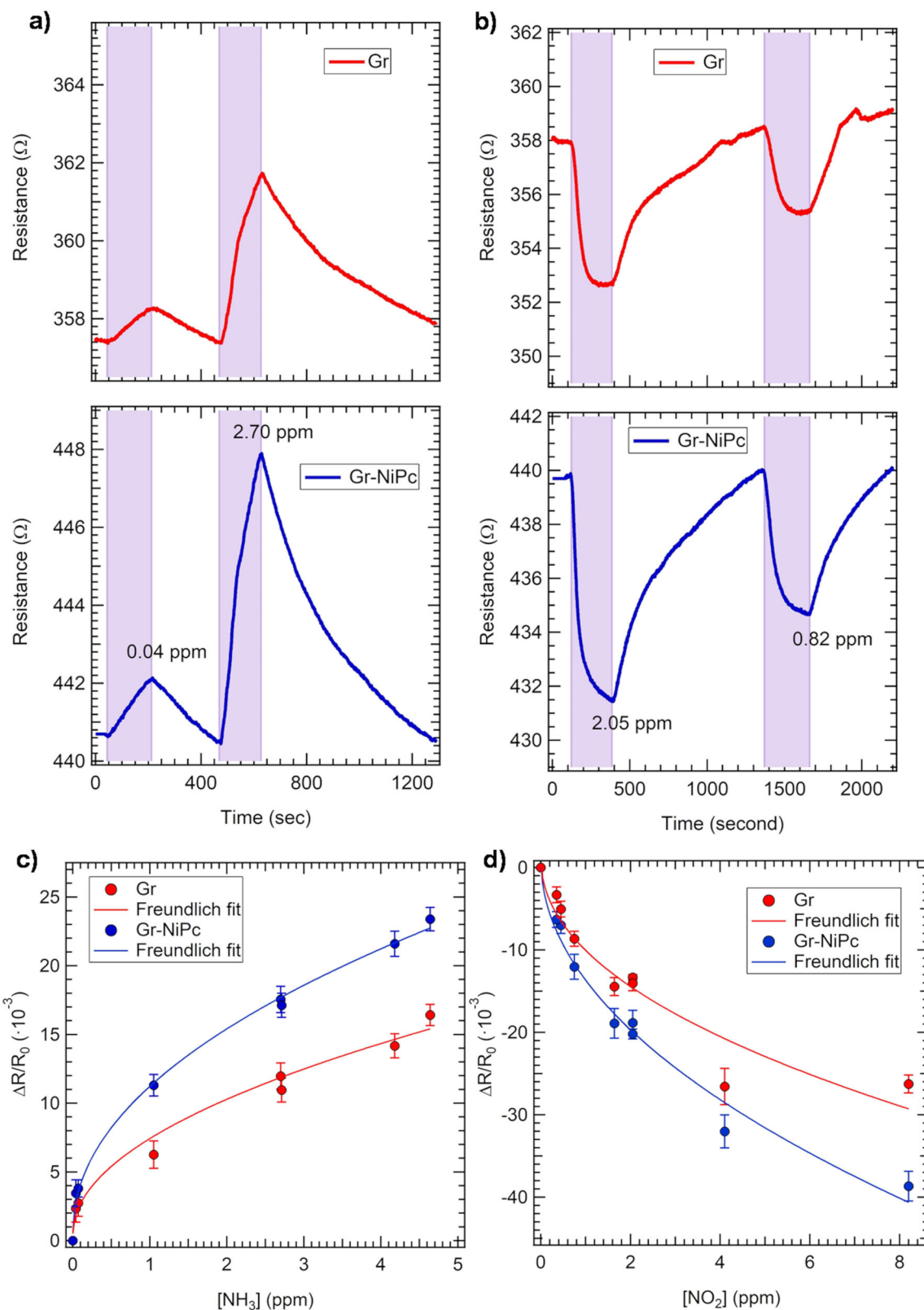
Fig. 7 | Gas exposures to ammonia and nitrogen dioxide. Response of the Gr (red) and Gr–NiPc (blue) to (**a**) 0.04 ppm and 2.7 ppm of ammonia and **b** 2.05 ppm and 0.82 ppm of nitrogen dioxide. The shaded areas indicate the exposure time: 3 min for ammonia and 5 min for nitrogen dioxide. Of note: the resistance range is the same for both samples, for ammonia (9 Ω) and nitrogen dioxide (12 Ω). Calibration curves extracted from several measurements upon ammonia (**c**) and nitrogen dioxide (**d**) exposures for Gr (red curve) and Gr–NiPc (blue curve) samples. Error bars are estimated on the basis of the signal-to-noise ratio.

Fig. 8 | Benchmarking for sensitivity of graphene-based chemiresistors for NH$_3$ and NO$_2$ exposure. Benchmarking for the sensitivity parameter S, $(S = \frac{(\frac{\Delta R}{R_0} \times 100)}{[gas]})$ upon ammonia (**a**) and nitrogen dioxide (**b**) exposures of the prepared samples (blue and red dots) with respect to other graphene-based chemiresistor sensitivity values reported in the literature (black symbols)[21,38,48–71]. Data are presented with a log–log scale.
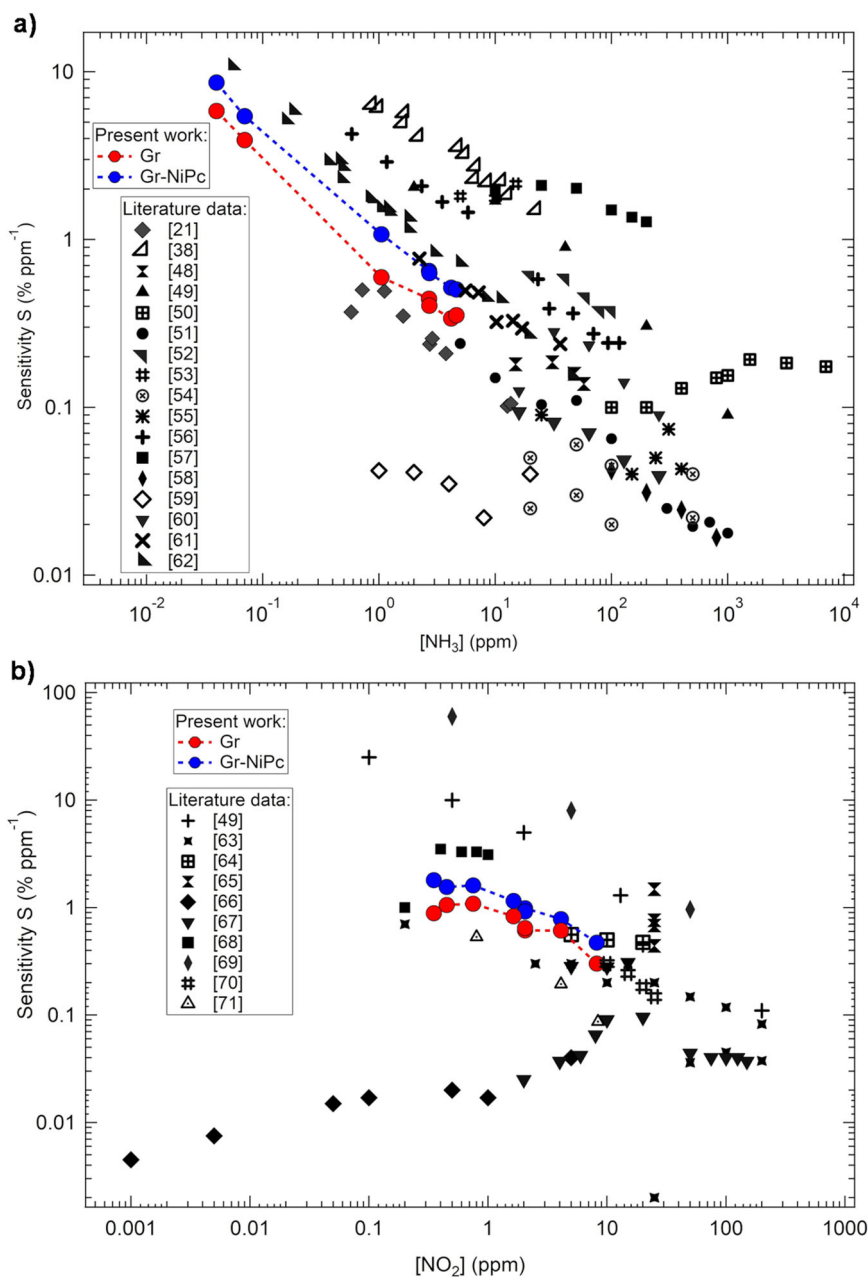
according to a protocol previously established by our group[78] to ammonia, acetone, nitrogen dioxide, water vapor, ethanol, ammonia + acetone, and ammonia + nitrogen dioxide mixtures, considering different relative concentration of the two gases. The results, reported in Supplementary Fig. S15, confirm the capability of the device to discriminate mixtures.

Finally, we proved the stability of the sensor signal in the absence of gases for the as-prepared samples (before and after NiPc deposition) and after 5 months from preparation (Supplementary Fig. S16). The reproducibility of the sensor response (Supplementary Fig. S17) and the failure error of the device performance are discussed in Section 5 of Supplementary Information.

Conclusions

In this work, which aimed at the design of highly responsive gas-sensing materials, we investigated the heterointerface formed by a monolayer of NiPc molecules supported on p-type doped graphene by means of state-of-the-art DFT calculations. This system was explored for its sensing response properties towards both electron donor (NH$_3$) and acceptor (NO$_2$) gases. To complement this theoretical study, which strongly points to the high

potential of this system for an effective and responsive chemiresistor device, we performed a proof-of-concept experiment where we prepared and tested the Gr–NiPc interface samples for their sensitivity toward the two different types of gases.

We started the computational investigation by exploring the adsorption modes of each gas molecule, considering two possible coverage regimes, in line with the experimental conditions. From these configurations, we delved into the gas effect on the electronic properties of the interface to establish the potential of this system for gas-sensing applications. In particular, we found that the presence of the metal is crucial, as we identified the filled Ni d_z^2 orbital of NiPc as a key player in the sensing mechanism, serving as a charge transfer channel between the gas molecules and the Gr layer. This mechanism is driven by the nature of the Ni d_z^2 orbital, which not only readily interacts with the frontier molecular orbitals of the chemical species present in the environment (HOMO and LUMO of NH$_3$ and NO$_2$, respectively), but also couples with the metallic π states of Gr, thus enabling the transfer of electrons across the interface.

Next, as a proof-of-concept for our theoretical investigation, we synthesized the Gr–NiPc system and tested its ability to detect ammonia and

nitrogen dioxide. The morphology and chemical composition of the Gr–NiPc system were assessed using Raman spectroscopy, XPS, and AFM. Raman and XPS techniques confirmed the successful deposition of intact NiPc molecules, while AFM images revealed the formation of a complete monolayer of NiPc molecules, along with some double-layer regions as a result of the nominal coverage of 1.5 monolayers of deposited molecules.

Subsequent tests on the system involved exposing it to electron-donor (NH_3) and electron-acceptor (NO_2) gas species were conducted. Given the p-doped nature of Gr–NiPc, we observed the electrical resistance of the system to increase or decrease in the presence of electron-donating or -withdrawing molecules, respectively. Comparing our results with available literature data underscores the remarkable sensing capabilities of the Gr–NiPc interface for both gases, confirming our theoretical predictions. Furthermore, our experimental findings highlight not only the high sensitivity of Gr–NiPc but also its good recovery time, low detection limit, and selectivity.

Finally, it is important to emphasize that comprehending the mechanistic details of the sensing process is of fundamental importance for the further development of effective and responsive graphene-based systems for sensing applications. In this study, we designed a NiPc-functionalized graphene system that exhibits promising sensing performance, unraveled the mechanistic details governing the system's response, and provided the proof-of-concept experiment. As a result, we believe that these findings can provide impetus for future investigations into functionalized graphene-based systems, aiming to achieve even superior outcomes. For instance, we observed that the role of the metal is crucial in mediating communication between the molecule and the Gr layer. Consequently, a different metal phthalocyanine may exhibit distinct behavior.

Methods
Computational methods
The spin-polarized DFT + U calculations have been performed using the plane-wave-based Quantum ESPRESSO package (QE)[79–81]. The ultrasoft pseudopotentials have been adopted to describe the electron-ion interactions with H ($1s$), Ni ($4s$, $3d$), C ($2s$, $2p$), N ($2s$, $2p$) and O ($2s$, $2p$) treated as valence electrons[82]. Energy cutoffs of 46 and 326 Ry (for kinetic energy and charge density expansion, respectively) have been adopted for all calculations. The Perdew–Burke–Ernzerhof functional (PBE) was employed for electron exchange-correlation[83], and semiempirical corrections accounting for van der Waals interactions were included using the DFT-D3 formalism[84]. To determine an appropriate U value, we tested values ranging from 3 eV to 8 eV on the electronic properties of Gr–NiPc systems. Despite this range, our results (illustrated in Supplementary Fig. 18) reveal no influence of U on charge transfer at the Gr–NiPc interface (red dots), as it primarily depends on the aromatic part of the molecule (Pc) rather than the metal center (Ni).

Differently, U significantly influences charge transfer between the gas-phase molecule and Gr–NiPc (blue dots in Supplementary Fig. 18), involving Ni's d orbitals. Without U, we observe maximum charge transfer from NH_3 to Gr. Increasing U results in a linear decrease, with no transfer at U = 8. Considering literature values in the range of 3–5 eV[85,86], we selected a value of U = 5 eV for all calculations. This choice provides an intermediate value of the transfer, avoiding potential spurious extremes.

The convergence criterion of 0.026 eV/Å for the forces has been used during geometry optimization, and the convergence criterion for the total energy has been set at 10^{-6} Ry. Spin polarization was included when needed.

To model graphene, a supercell with dimensions ($\sqrt{31} \times \sqrt{28}$) R9, containing 68 carbon atoms, was used (for more details, see Supplementary Fig. 19). In this model, the available graphene surface area is approximately 1.78 nm². The Gr–NiPc interface was built by placing one NiPc molecule on graphene. For geometry relaxation and density of states (DOS) calculations, Monkhorst–Pack[87] k-points meshes of $6 \times 6 \times 1$ and $18 \times 18 \times 1$ were employed, respectively. A vacuum space of 25 Å was included in the supercell model to prevent interactions between adjacent periodic images. A dipole correction was applied to account for field effects.

To build a computational model of a free-standing p-type doped graphene layer, all calculations were charged by removing a specific number of electrons (e) from the system. In particular, we considered two distinct doping conditions by removing a different number of electrons from the cell: 0.18 e (low doping) and 0.72 e (high doping).

Sample preparation and characterization
Graphene on 4H-SiC samples has been purchased from Graphensic[88], whereas nickel phthalocyanine (NiPc) powder (98%) has been bought from Alfa Aesar. Graphene has been declared as a monolayer with a 25% probability of bilayer nature from the producer. The cleaning procedure of the Gr sample has been performed with 5 flash annealing cycles at 450 °C for 2 min each. To functionalize the graphene layer, NiPc has been sublimated in UHV with a custom-made thermal evaporator, built of a quartz crucible allocated on a water-cooled cryo panel, and deposited on a clean kept at ambient temperature. The deposition rate has been monitored by a homemade quartz oscillator (≈3.65 Å, in about 1 min) and a thermocouple has been inserted in the crucible. A cross-sectional sketch of the layers, after the deposition of silver contact to perform gas measurements, is reported in Supplementary Fig. 20a.

Atomic force microscopy (AFM) images have been acquired with a Park NX 10 AFM system in the tapping mode, with a tip (PPP-NCHR-50 by NanoSensors) operating at a resonance frequency of about 160 kHz (force constant: 8 Nm⁻¹). Image processing has been carried out using the Gwyddion software[89].

Raman spectra and micro-Raman maps have been collected with a Renishaw-Invia system, equipped with a 633 nm laser source. The laser light has been always focused onto the sample with a 100× objective. An 1800 lines/mm grating and a laser power of 2.5 mW have been used for the measurements.

X-ray photoemission spectroscopy (XPS) data have been collected at the UHV chamber of the ALOISA beamline[90] of the Elettra synchrotron in Trieste. X-ray photoemission spectra have been collected with the sample at a grazing angle of 3.0° (p-polarization) and normal emission, by means of a hemispherical analyzer (mean radius of 66 mm, acceptance angle of ~2° FWHM) equipped with a 2D delay line detector. The XP spectra were acquired at photon energies of 515 eV (N $1s$, C $1s$, Si $2p$) and 1030 eV (Ni $2p$, Si $2p$). The photoemission spectra have been calibrated to the binding energy of Si $2p_{3/2}$ of the SiC substrate at 101.3 eV. Voigt functions have been used to fit the XPS data.

Gas sensor measurements
Electrical contacts made of silver paint have been printed as small stripes on the opposite sides of a pristine sample and on the functionalized layer.

The graphene layers are on a 7 mm×7 mm SiC substrate purchased from Graphensic. The Ag electrodes made of silver paint are 6 mm×1 mm each, and the distance between the electrodes is about 4 mm. The thickness of the SiC substrate is (500 ± 25) μm, while the graphene layer is about 1 nm, according to the producer. The film thickness as well as the electrode size can influence the electrical properties and the resistance of the sensor, nevertheless, as will be proven in the next paragraphs and in the manuscript, the electrical signal collected between the two electrodes is stable and reproducible over time (at least 5 months), therefore we can assert that in this condition the sensor performances are controllable.

Both samples, mounted on a properly designed platform, work simultaneously, allowing a direct comparison of the behavior of the sensors under the same environmental conditions. Two commercial sensors have been put on the platform: a relative humidity (RH) sensor (humidity sensor HIH-4000 series—Honeywell Sensing) and a temperature sensor (Thermistor NTC PCB 5 K—Murata). In the case of ammonia exposures, an additional commercially available chemiresistor sensor (Figaro, TGS 2602) is mounted on the platform to cross-check the gas concentration. A schematic representation of the platform and its components is reported in Supplementary Fig. 20b.

The developed graphene-based sensors work in a chemiresistor configuration (readout scheme in Supplementary Fig. 20c): the gas analytes are detected by measuring the resistance changes of the sensing layers induced by the interaction with the gas molecules; the electronic circuit of each sensor comprises a load resistor (R_L) is in series with the sensor and by applying a constant voltage (5 V) and monitoring the output voltage across the sample (V_{OUT}), it is possible to track the resistance R of the sensor. The response of the sensor is then defined as $\Delta R/R_0 = (R - R_0)/R_0$, where R_0 is the baseline sensor resistance before the gas exposure, and $\Delta R = R - R_0$ is the resistance variation due to the interaction with the gas molecules. Nitrogen dioxide and ammonia exposures have been carried out at room temperature in a sealed chamber.

In detail, two chambers with different volumes have been used for the exposures to ammonia and nitrogen dioxide, 0.75 l and 1.5 l. Based on the incoming flux and fluid dynamics inside the chambers, 3 min and 5 min are the estimated times required for the gas to completely saturate the two chambers. Therefore, in this way, we were able to correctly establish the concentration of the target gas, since a steady-state concentration was always reached. As mentioned, NH_3 concentration was cross-checked with a Figaro sensor during each exposure. Finally, the minimum time required for the detection of NH_3 and NO_2 is influenced by several parameters, including the chamber geometry and the flux selected for the exposures[46]. Therefore, in our operating conditions, 3 min and 5 min can be considered as the minimum time values required for a correct detection. Exploiting a chamber with a smaller volume and/or using a higher gas flux, the minimum time for gas detection can be lower.

Both chambers are connected with two mass-flow controllers (MFCs), which in turn are connected to a cylinder containing synthetic air (oxygen 21%, nitrogen 79%), and to a cylinder of the gas analyte diluted in synthetic air (certified by S.I.A.D. S.p.A.). The MCF connected to the dry air cylinder has a maximum flow of 1000 sccm, while the max flow of the MFC connected to the analyte cylinders is 500 sccm. In all the gas measurements, synthetic air has been used for both chamber purge after the exposure and to dilute the analyte in order to obtain different concentration exposures. Supplementary Fig. 20d shows the setup exploited for the gas exposures. Considering several exposures, calibration curves for each sensor could be obtained by plotting the sensor response $\Delta R/R_0$ vs the gas concentration.

Data availability
All data shown in the main text and supplementary information are available from the corresponding authors upon request.

References
1. Milone, A. et al. Advances in materials and technologies for gas sensing from environmental and food monitoring to breath analysis. *Adv. Sustain. Syst.* **7**, 2200083 (2023).
2. Banga, I., Paul, A., Poudyal, D. C., Muthukumar, S. & Prasad, S. Recent advances in gas detection methodologies with a special focus on environmental sensing and health monitoring applications—a critical review. *ACS Sens.* **8**, 3307–3319 (2023).
3. Berwal, P. et al. Hybrid metal oxide nanocomposites for gas-sensing applications: a review. *Ind. Eng. Chem. Res.* **62**, 14835–14852 (2023).
4. Bhati, V. S., Kumar, M. & Banerjee, R. Gas sensing performance of 2D nanomaterials/metal oxide nanocomposites: a review. *J. Mater. Chem. C.* **9**, 8776–8808 (2021).
5. Nikolic, M. V., Milovanovic, V., Vasiljevic, Z. Z. & Stamenkovic, Z. Semiconductor gas sensors: materials, technology, design, and application. *Sensors* **20**, 6694 (2020).
6. Dey, A. Semiconductor metal oxide gas sensors: a review. *Mater. Sci. Eng. B* **229**, 206–217 (2018).
7. Wang, Z., Bu, M., Hu, N. & Zhao, L. An overview on room-temperature chemiresistor gas sensors based on 2D materials: research status and challenge. *Compos. Part B Eng.* **248**, 110378 (2023).
8. Paghi, A., Mariani, S. & Barillaro, G. 1D and 2D field effect transistors in gas sensing: a comprehensive review. *Small* **19**, 2206100 (2023).
9. Perilli, D., Selli, D., Liu, H., Bianchetti, E. & Di Valentin, C. h-BN defective layers as giant N-donor macrocycles for Cu adatom trapping from the underlying metal substrate. *J. Phys. Chem. C.* **122**, 23610–23622 (2018).
10. Ji, H., Zeng, W. & Li, Y. Gas sensing mechanisms of metal oxide semiconductors: a focus review. *Nanoscale* **11**, 22664–22684 (2019).
11. Casotto, A. et al. π-Orbital mediated charge transfer channels in a monolayer Gr–NiPc heterointerface unveiled by soft X-ray electron spectroscopies and DFT calculations. *Nanoscale* **14**, 13166–13177 (2022).
12. Gounden, D., Nombona, N. & Van Zyl, W. E. Recent advances in phthalocyanines for chemical sensor, non-linear optics (NLO) and energy storage applications. *Coord. Chem. Rev.* **420**, 213359 (2020).
13. Wu, H. et al. Stably dispersed carbon nanotubes covalently bonded to phthalocyanine cobalt (II) for ppb-level H_2S sensing at room temperature. *J. Mater. Chem. A* **4**, 1096–1104 (2016).
14. Liu, Q., Gao, L., Su, X., Zhou, F. & Duan, G. Interfacial self-assembly of CoPc thin films with their high sensing use as NO_2 sensors. *Mater. Chem. Phys.* **234**, 94–101 (2019).
15. Kumar, S., Kaur, N., Sharma, A. K., Mahajan, A. & Bedi, R. K. Improved Cl_2 sensing characteristics of reduced graphene oxide when decorated with copper phthalocyanine nanoflowers. *RSC Adv.* **7**, 25229–25236 (2017).
16. Zhu, Y. et al. High-performance NO_2 sensors based on ultrathin heterogeneous interface layers. *Adv. Mater. Interfaces* **7**, 1901579 (2020).
17. Urbani, M., Ragoussi, M. E., Nazeeruddin, M. K. & Torres, T. Phthalocyanines for dye-sensitized solar cells. *Coord. Chem. Rev.* **381**, 1–64 (2019).
18. Lo, P. C. et al. The unique features and promises of phthalocyanines as advanced photosensitisers for photodynamic therapy of cancer. *Chem. Soc. Rev.* **49**, 1041–1056 (2020).
19. Atxabal, A. et al. Spin doping using transition metal phthalocyanine molecules. *Nat. Commun.* **7**, 13751 (2016).
20. Yuan, S. et al. Tuning the catalytic activity of Fe-phthalocyanine-based catalysts for the oxygen reduction reaction by ligand functionalization. *ACS Catal.* **12**, 7278–7287 (2022).
21. Freddi, S., Marzuoli, C., Pagliara, S., Drera, G. & Sangaletti, L. Targeting biomarkers in the gas phase through a chemoresistive electronic nose based on graphene functionalized with metal phthalocyanines. *RSC Adv.* **13**, 251–263 (2023).
22. Calmeiro, J. M., Tomé, J. P. & Lourenço, L. M. Supramolecular graphene–phthalocyanine assemblies for technological breakthroughs. *J. Mater. Chem. C.* **8**, 8344–8361 (2020).
23. Novoselov, K. S. et al. A roadmap for graphene. *Nature* **490**, 192–200 (2012).
24. Cuxart, M. G. et al. Spatial segregation of substitutional B atoms in graphene patterned by the moiré superlattice on Ir (111). *Carbon* **201**, 881–890 (2023).
25. Georgakilas, V. et al. Noncovalent functionalization of graphene and graphene oxide for energy materials, biosensing, catalytic, and biomedical applications. *Chem. Rev.* **116**, 5464–5519 (2016).
26. Altenburg, S. J., Lattelais, M., Wang, B., Bocquet, M. L. & Berndt, R. Reaction of phthalocyanines with graphene on Ir (111). *J. Am. Chem. Soc.* **137**, 9452–9458 (2015).
27. Yang, K. et al. Molecule–substrate coupling between metal phthalocyanines and epitaxial graphene grown on Ru (0001) and Pt (111). *J. Phys. Chem. C.* **116**, 14052–14056 (2012).
28. Ren, J. et al. Properties of copper (fluoro-) phthalocyanine layers deposited on epitaxial graphene. *J. Chem. Phys.* **134**, 194706 (2011).

29. Dieng, M. et al. Wet-chemical noncovalent functionalization of CVD graphene: molecular doping and its effect on electrolyte-gated graphene field-effect transistor characteristics. *J. Phys. Chem. C.* **126**, 4522–4533 (2022).

30. Zemła, M. R., Czelej, K. & Majewski, J. A. Graphene–Iron (II) phthalocyanine hybrid systems for scalable molecular spintronics. *J. Phys. Chem. C.* **124**, 27645–27655 (2020).

31. Feng, S. et al. Phthalocyanine and metal phthalocyanines adsorbed on graphene: a density functional study. *J. Phys. Chem. C.* **123**, 16614–16620 (2019).

32. Yin, H., Lin, H., Zhang, Y. & Huang, S. Iron (II) phthalocyanine adsorbed on defective graphenes: a density functional study. *ACS Omega* **7**, 43915–43922 (2022).

33. Goswami, P. & Gupta, G. Recent progress of flexible NO₂ and NH₃ gas sensors based on transition metal dichalcogenides for room temperature sensing. *Mater. Today Chem.* **23**, 100726 (2022).

34. Wagner, J., Jang, H. J., Han, J. & Katz, H. E. Enhanced and unconventional responses in chemiresistive sensing devices for nitrogen dioxide and ammonia from carboxylated alkylthiophene polymers. *Mater. Horiz.* **7**, 1358–1371 (2020).

35. Das, S. & Pal, M. Non-invasive monitoring of human health by exhaled breath analysis: a comprehensive review. *J. Electrochem. Soc.* **167**, 037562 (2020).

36. Freddi, S. & Sangaletti, L. Trends in the development of electronic noses based on carbon nanotubes chemiresistors for breathomics. *Nanomaterials* **12**, 2992 (2022).

37. Annanouch, F. E. et al. Controlled growth of 3D assemblies of edge enriched multilayer MoS 2 nanosheets for dually selective NH₃ and NO₂ gas sensors. *J. Mater. Chem. C.* **10**, 11027–11039 (2022).

38. Freddi, S. et al. Pushing down the limit of NH₃ detection of graphene-based chemiresistive sensors through functionalization by thermally activated tetrazoles dimerization. *ACS Nano* **16**, 10456–10469 (2022).

39. Del Puppo, S. et al. Tuning graphene doping by carbon monoxide intercalation at the Ni (111) interface. *Carbon* **176**, 253–261 (2021).

40. Joucken, F. et al. Charge transfer and electronic doping in nitrogen-doped graphene. *Sci. Rep.* **5**, 14564 (2015).

41. Carné-Sánchez, A. et al. Ammonia capture in rhodium (II)-based metal–organic polyhedra via synergistic coordinative and H-bonding interactions. *ACS Appl. Mater. Interfaces* **15**, 6747–6754 (2023).

42. Hammer, B. & Norskov, J. K. Why gold is the noblest of all the metals. *Nature* **376**, 238–240 (1995).

43. Ferrari, A. C. & Basko, D. M. Raman spectroscopy as a versatile tool for studying the properties of graphene. *Nat. Nanotechnol.* **8**, 235–246 (2013).

44. Ni, Z. H. et al. Raman spectroscopy of epitaxial graphene on a SiC substrate. *Phys. Rev. B* **77**, 115416 (2008).

45. Ferrari, A. C. et al. Raman spectrum of graphene and graphene layers. *Phys. Rev. Lett.* **97**, 187401 (2006).

46. Galvani, M., Freddi, S. & Sangaletti, L. Disclosing fast detection opportunities with nanostructured chemiresistor gas sensors based on metal oxides, carbon, and transition metal dichalcogenides. *Sensors* **24**, 0 (2024).

47. Freddi, S. et al. Development of a sensing array for human breath analysis based on swcnt layers functionalized with semiconductor organic molecules. *Adv. Healthc. Mater.* **9**, 2000377 (2020).

48. Gautam, M. & Jayatissa, A. H. Ammonia gas sensing behavior of graphene surface decorated with gold nanoparticles. *Solid-State Electron.* **78**, 159–165 (2012).

49. Yavari, F., Castillo, E., Gullapalli, H., Ajayan, P. M. & Koratkar, N. High sensitivity detection of NO₂ and NH₃ in air using chemical vapor deposition grown graphene. *Appl. Phys. Lett.* **100**, 20 (2012).

50. Wu, Z. et al. Enhanced sensitivity of ammonia sensor using graphene/polyaniline nanocomposite. *Sens. Actuators B Chem.* **178**, 485–493 (2013).

51. Seekaew, Y. et al. Low-cost and flexible printed graphene–PEDOT: PSS gas sensor for ammonia detection. *Org. Electron.* **15**, 2971–2981 (2014).

52. Li, Q. et al. Highly sensitive graphene-based ammonia sensor enhanced by electrophoretic deposition of MXene. *Carbon* **202**, 561–570 (2023).

53. Jagannathan, M., Dhinasekaran, D., Rajendran, A. R. & Subramaniam, B. Selective room temperature ammonia gas sensor using nanostructured ZnO/CuO@ graphene on paper substrate. *Sens. Actuators B Chem.* **350**, 130833 (2022).

54. Ben Aziza, Z., Zhang, Q., & Baillargeat, D. Graphene/mica based ammonia gas sensors. *Appl. Phys. Lett.* **105**, 254102 (2014).

55. Wu, D. et al. A simple graphene NH₃ gas sensor via laser direct writing. *Sensors* **18**, 4405 (2018).

56. Li, Q. et al. Highly sensitive graphene ammonia sensor enhanced by concentrated nitric acid treatment. *Appl. Surf. Sci.* **586**, 152689 (2022).

57. Xiang, C. et al. Ammonia sensor based on polypyrrole–graphene nanocomposite decorated with titania nanoparticles. *Ceram. Int.* **41**, 6432–6438 (2015).

58. Liang, T. et al. Preparation and test of NH₃ gas sensor based on single-layer graphene film. *Micromachines* **11**, 965 (2020).

59. Lv, R. et al. Ultrasensitive gas detection of large-area boron-doped graphene. *Proc. Natl. Acad. Sci. USA* **112**, 14527–14532 (2015).

60. Srivastava, S., Jain, S. K., Gupta, G., Senguttuvan, T. D. & Gupta, B. K. Boron-doped few-layer graphene nanosheet gas sensor for enhanced ammonia sensing at room temperature. *RSC Adv.* **10**, 1007–1014 (2020).

61. Freddi, S., Vergari, M., Pagliara, S. & Sangaletti, L. A chemiresistor sensor array based on graphene nanostructures: from the detection of ammonia and possible interfering VOCs to chemometric analysis. *Sensors* **23**, 882 (2023).

62. Freddi, S., Gonzalez, M. C. R., Carro, P., Sangaletti, L. & De Feyter, S. Chemical defect-driven response on graphene-based chemiresistors for sub-ppm ammonia detection. *Angew. Chem. Int. Ed.* **61**, e202200115 (2022).

63. Chung, M. G. et al. Highly sensitive NO₂ gas sensor based on ozone treated graphene. *Sens. Actuators B Chem.* **166**, 172–176 (2012).

64. Srivastava, V. & Jain, K. At room temperature graphene/SnO₂ is better than MWCNT/SnO₂ as NO₂ gas sensor. *Mater. Lett.* **169**, 28–32 (2016).

65. Seekaew, Y., Phokharatkul, D., Wisitsoraat, A. & Wongchoosuk, C. Highly sensitive and selective room-temperature NO₂ gas sensor based on bilayer transferred chemical vapor deposited graphene. *Appl. Surf. Sci.* **404**, 357–363 (2017).

66. Guo, L. & Li, T. Sub-ppb and ultra selective nitrogen dioxide sensor based on sulfur doped graphene. *Sens. Actuators B Chem.* **255**, 2258–2263 (2018).

67. Yan, X. et al. High-performance UV-assisted NO₂ sensor based on chemical vapor deposition graphene at room temperature. *ACS Omega* **4**, 14179−14187 (2019).

68. Gupta, R. K. et al. Suspended graphene arrays for gas sensing applications. *2D Mater* **8**, 025006 (2020).

69. Ying, S. et al. Highly-sensitive NO₂ gas sensors based on three-dimensional nanotube graphene and ZnO nanospheres nanocomposite at room temperature. *Appl. Surf. Sci.* **566**, 150720 (2021).

70. Lee, K. S. et al. Adsorption behavior of NO₂ molecules in ZnO-mono/multilayer graphene core–shell quantum dots for NO₂ gas sensor. *J. Ind. Eng. Chem.* **106**, 279–286 (2022).

71. Freddi, S., Rodriguez Gonzalez, M. C., Casotto, A., Sangaletti, L. & De Feyter, S. Machine-learning-aided NO₂ discrimination with an array of graphene chemiresistors covalently functionalized by diazonium chemistry. *Chem. A Eur. J.* **29**, e202302154 (2023).

72. Kumar, D. et al. Effect of single wall carbon nanotube networks on gas sensor response and detection limit. *Sens. Actuators B* **240**, 1134–1140 (2017).

73. Wen, Y. et al. A covalent organic–inorganic hybrid superlattice covered with organic functional groups for highly sensitive and selective gas sensing. *Angew. Chem. Int. Ed.* **60**, 19710–19714 (2021).

74. Zheng, W. et al. MoS2 Van der Waals p–n junctions enabling highly selective room-temperature NO_2 sensor. *Adv. Funct. Mater.* **30**, 2000435 (2020).

75. Lee, J. E. et al. ZnO–CuO core-hollow cube nanostructures for highly sensitive acetone gas sensors at the ppb level. *ACS Appl. Mater. Interfaces* **12**, 35688–35697 (2020).

76. Yang, Y., Wang, X., Zhao, L., Li, Z. & Sun, Y. An E-nose system for identification and quantification of hazardous gas mixtures using a combined strategy of CNNs and attentional mechanisms. *Phys. Scr.* **99**, 096001 (2024).

77. Sinju, K. R., Bhangare, B. K., Debnath, A. K. & Ramgir, N. S. Discrimination of binary mixture of toxic gases using ZnO nanowires-based E-nose. *J. Mater. Sci. Mater. Electron.* **34**, 1562 (2023).

78. Freddi, S., Drera, G., Pagliara, S., Goldoni, A. & Sangaletti, L. Enhanced selectivity of target gas molecules through a minimal array of gas sensors based on nanoparticle-decorated SWCNTs. *Analyst* **144**, 4100–4110 (2019).

79. Giannozzi, P. et al. QUANTUM ESPRESSO: a modular and open-source software project for quantum simulations of materials. *J. Phys. Condens. Matter* **21**, 395502 (2009).

80. Giannozzi, P. et al. Advanced capabilities for materials modelling with Quantum ESPRESSO. *J. Phys. Condens. Matter* **29**, 465901 (2017).

81. Cococcioni, M. & De Gironcoli, S. Linear response approach to the calculation of the effective interaction parameters in the LDA + U method. *Phys. Rev. B* **71**, 035105 (2005).

82. Dal Corso, A. Pseudopotentials periodic table: from H to Pu. *Comput. Mater. Sci.* **95**, 337–350 (2014).

83. Perdew, J. P., Burke, K. & Ernzerhof, M. Generalized gradient approximation made simple. *Phys. Rev. Lett.* **77**, 3865 (1996).

84. Grimme, S., Antony, J., Ehrlich, S. & Krieg, H. A consistent and accurate ab initio parametrization of density functional dispersion correction (DFT-D) for the 94 elements H–Pu. *J. Chem. Phys.* **132**, 154104 (2010).

85. Brumboiu, I. E. et al. Influence of electron correlation on the electronic structure and magnetism of transition-metal phthalocyanines. *J. Chem. Theory Comput.* **12**, 1772–1785 (2016).

86. Brumboiu, I. E. et al. Ligand effects on the linear response hubbard U: the case of transition metal phthalocyanines. *J. Phys. Chem. A* **123**, 3214–3222 (2019).

87. Monkhorst, H. J. & Pack, J. D. Special points for Brillouin-zone integrations. *Phys. Rev. B* **13**, 5188 (1976).

88. https://graphensic.com/.

89. Nečas, D. & Klapetek, P. Gwyddion: an open-source software for SPM data analysis. *Open Phys.* **10**, 181–188 (2012).

90. Floreano, L. et al. Performance of the grating-crystal monochromator of the ALOISA beamline at the elettra synchrotron. *Rev. Sci. Instrum.* **70**, 3855–3864 (1999).

Acknowledgements

Author contributions

D.P. and C.D.V. designed the models and simulations. D.P. carried out theoretical calculations. D.P. and C.D.V. analyzed the computational data. S.F. and L. Sangaletti designed the experiments. S.F., M.Z., A.C., G.D., L. Schio, S.P., and L. Sangaletti performed the experiments. S.F., A.C., and L. Sangaletti analyzed experimental results. D.P. and S.F. wrote the original draft. D.P., S.F., L. Sangaletti, and C.D.V. reviewed the manuscript. L. Sangaletti and C.D.V. supervised the project. L. Sangaletti and C.D.V. funding acquisition.

Competing interests

The authors declare no competing interests.

Additional information

Supplementary information The online version contains supplementary material available at https://doi.org/10.1038/s43246-024-00693-z.

Correspondence and requests for materials should be addressed to Luigi Sangaletti or Cristiana Di Valentin.

Peer review information *Communications materials* thanks Hyun-June Jang and the other, anonymous, reviewer(s) for their contribution to the peer review of this work. Primary Handling Editor: Aldo Isidori.

Reprints and permissions information is available at http://www.nature.com/reprints

Publisher's note Springer Nature remains neutral with regard to jurisdictional claims in published maps and institutional affiliations.